Electronic Supplementary Material (ESI) for Nanoscale

SUPPORTING INFORMATION

Structural diversity in iron oxide nanoparticle assemblies as directed by particle morphology and orientation

S. Disch et al.

1 X-ray Powder Diffraction

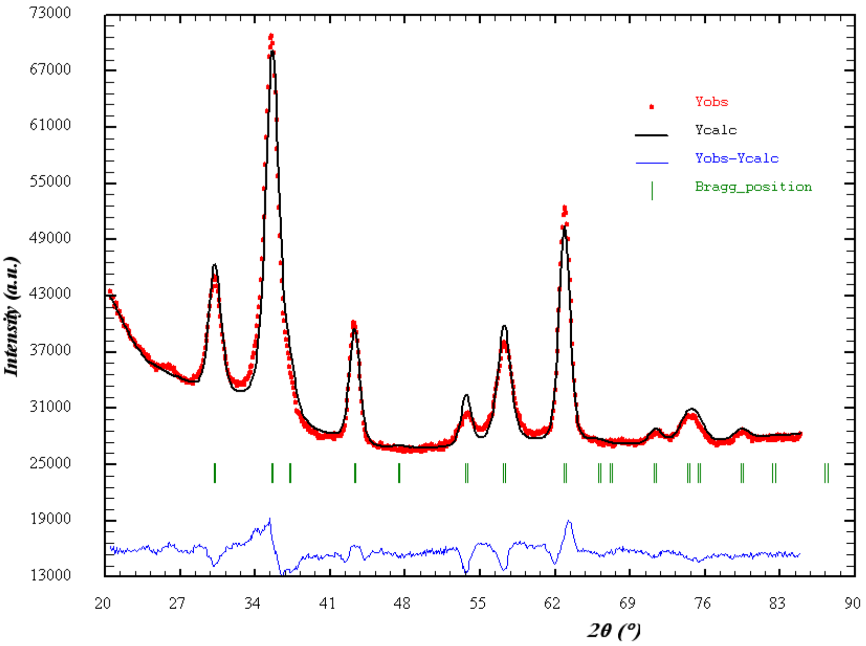

Figure S1: X-ray powder diffraction pattern of the iron oxide nanospheres sample.

X-ray Powder diffraction (XRPD) was measured on a conventional in-house powder diffractometer using Cu Kα radiation. Rietveld refinement yields cubic lattice parameters of 8.362(2) Å for the nanospheres and 8.348(1) Å for the nanocubes, which are both close to the cubic spinel lattice parameter of maghemite. The refined lattice parameter has further been used for calibration of the HRTEM images.

2 Transmission Electron Microscopy

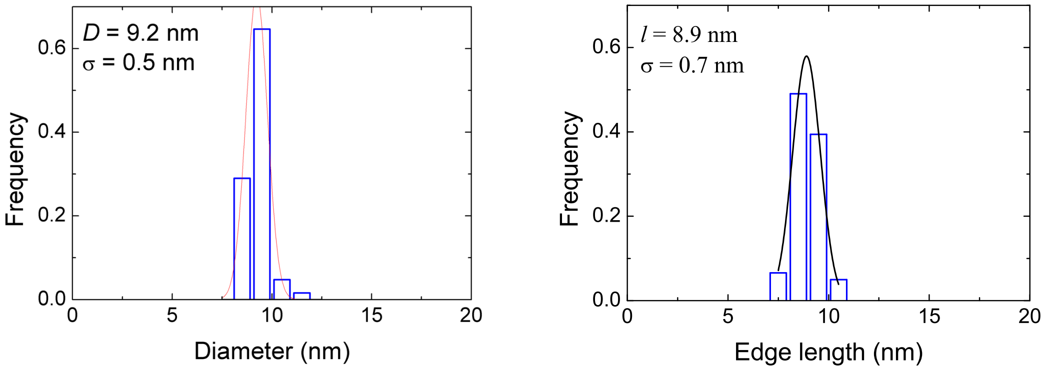

Figure S2: Particle size histograms corresponding to (left) spherical and (right) aged cubic nanoparticles, measured for > 200 nanospheres and > 50 nanocubes.

Figure S2 shows the histograms corresponding to the nanospheres and the aged nanocubes under study. As indicated in the figure, the analysis resulted in spherical and cubic particles with an average particle diameter, D = 9.2(4) nm, and an edge length, l = 8.9 nm, with Gaussian size distributions of σ = 0.5 nm and 0.7 nm, respectively.

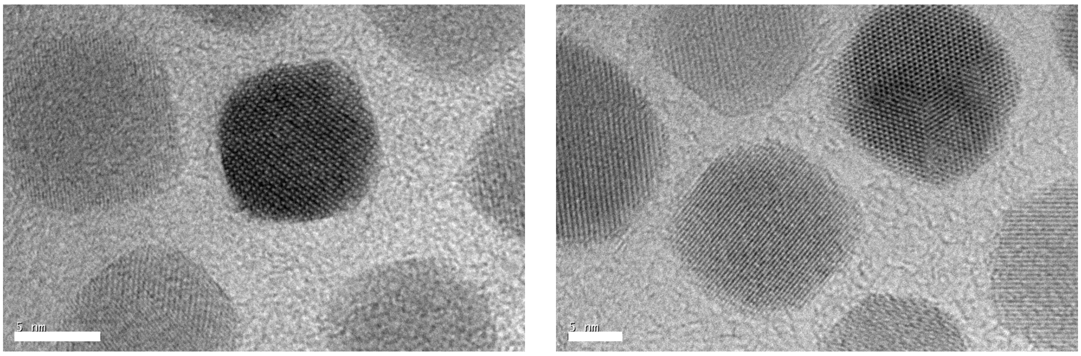

Figure S3: HRTEM images of cubic nanoparticles oriented close to the [100] zone axis (left) and oriented incorrectly (right). Scale bars correspond to 5 nm.

HRTEM images show that the cubes facets are terminated on the (100) planes and that both the corners and to a lesser extent the edges are truncated. The corners and edges correspond to the (111) and (110) planes of the spinel structure, respectively.

For the highly truncated nanocubes, four values of τ were obtained from each particle, and the histogram in Figure S4 is constructed from 280 τ values. As the figure indicates, a mean value for the degree of truncation, τ = 0.53 with a standard deviation, $\sigma_\tau = 0.07$ were obtained from fitting the histogram with a Gaussian distribution function.

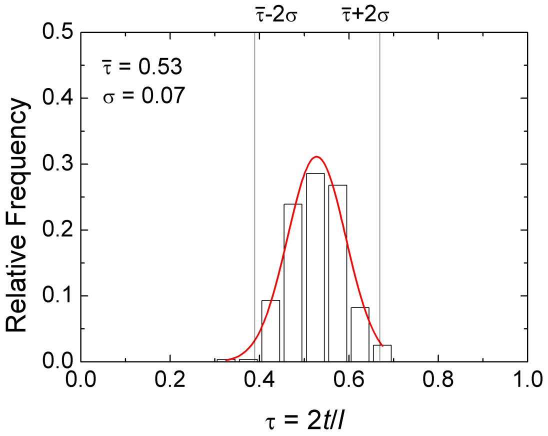

Figure S4: Histogram of the degree of truncation, manually measured for 70 particles (280 corners). The line shows a fit of the histogram according to a Gaussian distribution function.

For these measurements, particles oriented close to the [001] zone axis are required (see Figure S3). In essence this means that particles are selected based on preferential orientation which will cause an oversampling of more cube like particles with smaller τ. For the high degree of truncation in the studied samples, a large amount of nanocubes is oriented in the [111] direction, *i.e.* lying on the truncated facet, and only those nanocubes with a slightly lower degree of truncation are oriented favorably for determination of τ. This results in an oversampling of the nanocubes with a lower truncation. Nevertheless, even without considering an oversampling of cubic particles, the truncation of the aged sample studied here ($\tau = 0.53 \pm 0.07$) is significantly higher than before ($\tau = 0.45 \pm 0.05$).

3 Small-angle X-ray scattering

SAXS data of both nanospheres and nanocubes (Figure S5) were refined according to a spherical form factor. The nanospheres data sets reveal an excellent form factor behavior in the entire Q range. The deviation between the data and the fit for the aged nanocubes at small Q is due to the onset of a structure factor, and the small Q range was thus excluded for refinement. In order to take into account the resolution in the magnitude of the scattering vector, Q, a wavelength spread of $\Delta\lambda/\lambda = 5 \times 10^{-5}$ and an overall angular resolution parameter of $\mathrm{d}\theta = 0.3$ mrad were implemented in SAXS refinements of the data obtained with the Pilatus detector. As experimental parameters such as the beam size and sample thickness may also contribute to the Q resolution, the obtained particle size distribution can be regarded as the upper limit

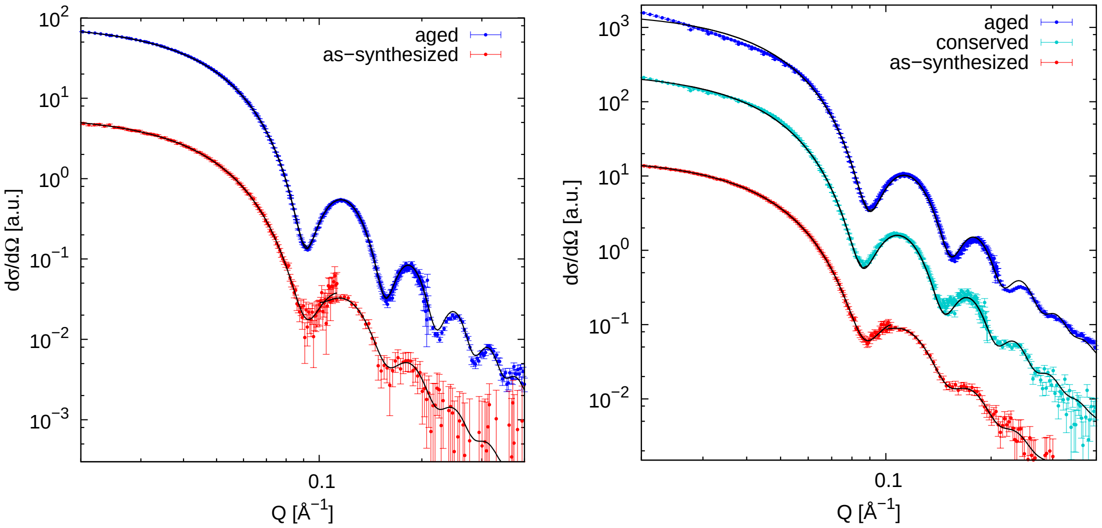

Figure S5: SAXS by iron oxide nanospheres (left) and nanocubes (right). Data have been scaled for display. The data marked as 'aged' has been measured 9 months later on the same sample. Nanocubes data labeled 'as-synthesized' and 'aged' corresponds to the 'truncated' and 'highly truncated' nanocubes data in Figure 1 (main text).

of the real particle size distribution. In order to account for the lower Q resolution of the Gabriel detector, the nanospheres sample (which did not reveal a significant change in particle size with time and was thus assumed to have a constant particle size distribution) was used as a calibrant, leading to angular resolution parameters of $d\theta = 0.55$ mrad and 0.95 mrad for the long and short distance, respectively.

A link between the spherical radius obtained using the spherical form factor and the cubic morphology is established using the radius of gyration, R_G, which may generally be obtained in the limit of low Q according to the Guinier approximation. The radius of gyration is given by $R_G^2 = \frac{3}{5}R_s^2$ for a dense sphere and $R_G^2 = \frac{1}{4}l_c^2$ for a perfect cubic particle. For a truncated cube, R_G depends on both the particle edge length l_c and the degree of truncation τ, two parameters which are highly correlated and thus cannot be determined independently. For a general object, the radius of gyration is given by

$$R_G \sim \int \rho(r) r^2 dr \tag{S1}$$

with $\rho(r)$ the spatial density of the object and r the distance from its center of mass. A calculation of $\rho(r)$ for truncated nanocubes of different degree of truncation is presented in Figure S6a. Integration of the spatial particle density according to equation (S1) yields the radius of gyration R_G of the truncated cube relative to R_G of a perfect cube of the same edge length (Fig. S6b). We find that $R_G(\tau)$ follows an inverse cubic behavior of

$$R_G(\tau) = R_G(0) \cdot (1 - 0.171\tau^3) \tag{S2}$$

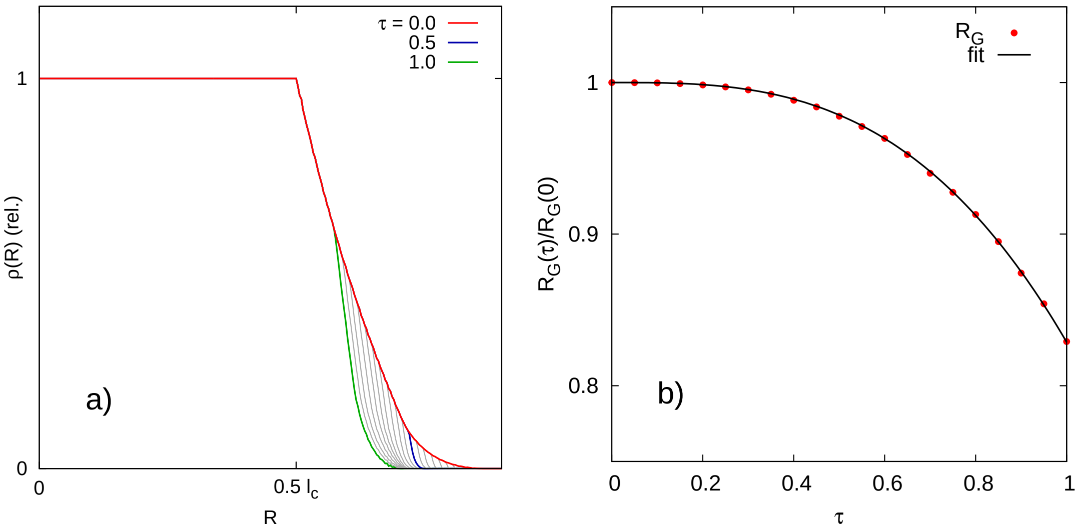

Figure S6: a) Orientationally averaged radial density in truncated nanocubes. b) Radius of gyration of truncated nanocubes relative to a perfect nanocube of the same edge length (points), described by Eq. S2 (line).

Table S1: Results of the SAXS refinement: spherical particle radius R_s, lognormal particle size distribution (FWHM) σ_{log}, and derived radius of gyration R_G for all nanospheres and nanocubes samples under study.

	nanospheres		nanocubes		
	as-synthesized	aged	as-synthesized	aged	conserved
R_s [Å]	50.3(3)	49.6(1)	53.2(2)	50.7(2)	52.9(3)
σ_{log}	0.056(5)	0.053(2)	0.07(1)	0.064(4)	0.07(1)
R_G [Å]	39.0(2)	38.4(2)	41.9(2)	39.3(2)	41.0(2)

SAXS refinement results using a spherical form factor are given in Table S1. The larger apparent particle size distribution of the nanocubes can be regarded as a result of the refinement approach. The non-spherical particle shape of the nanocubes is accommodated by an enlarged particle size distribution of the refined spherical form factor. The real particle size distribution of the truncated nanocubes will be lower and can, according to the TEM results, be expected in a similar range as for the spherical particles. A significant difference in particle size is observed for the as-synthesized and aged nanocubes, whereas the conserved nanocubes (a nanocubes sample stored in powder form in the dark) reveal a particle size similar to the original sample. For the as-synthesized nanocubes sample, the degree of truncation has been determined as 0.45(5). According to equation (S2), the measured radius of gyration corresponds to a $R_G(0)$ of 41.9(2) Å of the untruncated particle. This leads to a particle edge length of 83.8(4) Å, which is well in agreement with the edge length determined by TEM. For the aged nanocubes, the degree of truncation could not be determined precisely by TEM due to the orientational preference of the highly truncated nanocubes, and τ = 0.53(7) has been obtained as a lower limit of the real τ. The radius of gyration determined for the aged nanocubes, using with the edge length determined by HRTEM, yields a degree of truncation of τ = 0.88 according to equation (S2), which is as expected significantly larger than determined by TEM.

4 Mesocrystal structure determination

4.1 Nanospheres

GISAXS data have been analyzed as described earlier (Nano Lett. **11**, 1651 (2011).). The order parallel to the substrate is determined from the reflections in the Yoneda line, which contains the pure lateral structure information. The depth resolved mesocrystal structure is accessible through the Q_z position of the GISAXS reflections according to a combination of Snell's and Bragg's Laws.

The reflections in the Yoneda line of the nanospheres GISAXS data correspond to the hexagonal plane group *p6mm* for the lateral symmetry with a lattice constant of a = 12.4(1) nm. Indexing of the *hkl* GISAXS reflections in Figure 2 (main text) reveals a lattice constant perpendicular to the substrate of c = 29.5(1) nm. The observed extinction rule h - k + l = 3 n leads to a rhombohedral Bravais lattice. Note that the h and k indices of the observed reflections can not be distinguished for a 2 D powder of mesocrystals as studied here. Further, a comparison of the unit cell and individual nanoparticle volumes requires that only one special site is occupied by a nanosphere, leading to the rhombohedral space group $R\bar{3}m$ (No. 166).

For the three dimensional mesocrystal structure of the nanospheres, either *hcp* (ABAB), or *fcc* (ABCABC) type stacking or variants with stacking faults of the hexagonal monolayers were expected. By the found rhombohedral setting and extinction rules, GISAXS reveals a clear preference of the *fcc* stacking. The alternative of a *hcp* stacking type would correspond to the space group $P\ 6_3/m\ m\ c$ (No. 194) with a different extinction rule of $l = 2\,n$, which is unambiguously not observed. A comparison of observed and calculated reflection positions for the nanospheres mesocrystal structure is given in Table S2.

4.2 Highly truncated nanocubes

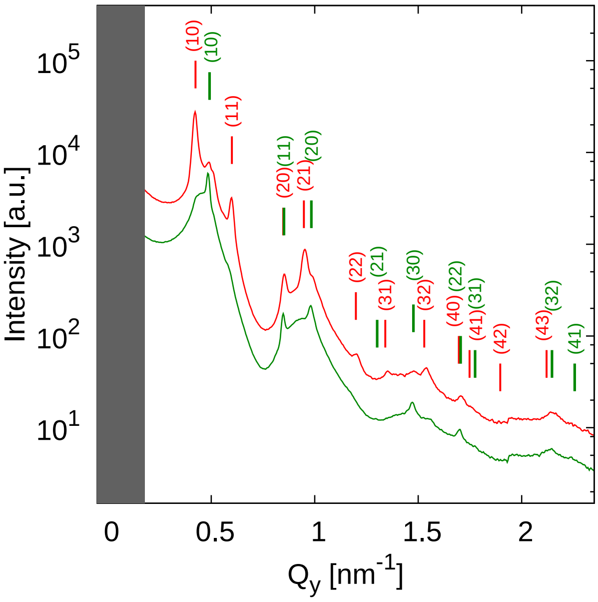

Figure S7: Comparison of the lateral scattering intensities (Yoneda line) of the GISAXS data exhibiting a preference of the tetragonal and rhombohedral configurations of the highly truncated mesocrystal structure (see Figure 3, main text). Reflections are indexed according to square (red) and hexagonal (green) lateral symmetry.

Figure S7 shows a comparison of the Yoneda line intensities in the GISAXS pattern with preferential [100] and [111] orientations of the *fcc* mesocrystal structure. The sharp reflections in the Yoneda line correspond to the square and hexagonal plane groups *p4mm* and *p6mm*, respectively, and their intensities illustrate the different ratios of the two structure orientations in different samples.

The GISAXS pattern presented in Figure 3 (main text) are shown again in Figure S8 without reflection markers, in order to give a clear view of the GISAXS reflections. A comparison of observed and calculated reflection positions for the *fcc* mesocrystal structure by highly truncated nanocubes in the [100] and [111] orientations is given in Tables S3 and S4, respectively. Both the tetragonal and rhombohedral lattice parameters obtained for the assemblies of highly truncated nanocubes are compatible with *fcc* stacking according to the relations illustrated in Figure S9.

For discussion of the possible nanoparticle orientations within the mesocrystals, the packing densities are determined from the particle morphology and the deter-

Table S2: List of GISAXS reflection positions parallel (Q_y) and perpendicular (Q_z) to the substrate for the nanospheres mesocrystals. The pattern was measured using an incident angle of 0.3° and indexed according to $R\bar{3}m$ with a = 12.4(1) nm and c = 29.5(1) nm.

Q_y[nm^{-1}]	$Q_{y,calc}$	Q_z[nm^{-1}]	$Q_{z,calc}$	*hkl* (▽)	*hkl* (△)
0.574(1)	0.585	0.306(1)	0.277	(011)	
0.574(1)		0.475(2)	0.455	(102)	
0.574(1)		0.593(1)	0.581		(011)
0.575(1)		0.799(1)	0.791		(102)
0.578(2)		0.871(2)	0.874	(014)	
0.579(2)		1.091(2)	1.086	(105)	
0.581(2)		1.223(2)	1.215		(014)
0.580(2)		1.432(2)	1.427		(105)
0.583(2)		1.719(2)	1.723	(108)	
0.586(2)		2.063(3)	2.065		(108)
0.589(2)		2.37(1)	2.361	(1.0.11)	
1.010(1)	1.013	0.383(1)	0.377	(110)	
1.010(1)		0.682(1)	0.663	(113)	
1.011(1)		1.008(1)	1.003		(113)
1.018(2)		1.326(2)	1.298	(116)	
1.020(1)		1.654(2)	1.64		(116)
1.164(1)	1.170	0.306(1)	0.277	(201)	
1.163(1)		0.473(2)	0.455	(022)	
1.164(1)		0.586(1)	0.581		(201)
1.164(1)		0.803(2)	0.791		(022)
1.166(1)		1.213(1)	1.215		(204)
1.173(1)		1.513(1)	1.51	(207)	
1.174(1)		1.719(3)	1.723	(028)	
1.173(2)		1.845(2)	1.853		(207)
1.171(2)		2.071(6)	2.065		(028)
1.174(2)		2.339(7)	2.361	(0.2.11)	
1.59(2)	1.548	0.357(5)	0.277	(121)	
1.554(2)		0.475(3)	0.455	(212)	
1.557(3)		0.808(4)	0.791		(212)
1.552(1)		0.888(2)	0.874	(124)	
1.554(2)		1.096(2)	1.086	(215)	
1.555(2)		1.209(4)	1.215		(124)
1.557(2)		1.425(3)	1.427		(215)
1.561(5)		2.144(5)	2.149	(1.2.10)	
1.758(1)	1.755	0.376(1)	0.377	(300)	
1.752(1)		0.670(2)	0.663	(303)	
1.757(2)		1.007(2)	1.003		(303)
1.763(5)		1.93(1)	1.94	(309)	
1.771(5)		2.26(2)	2.28		(309)

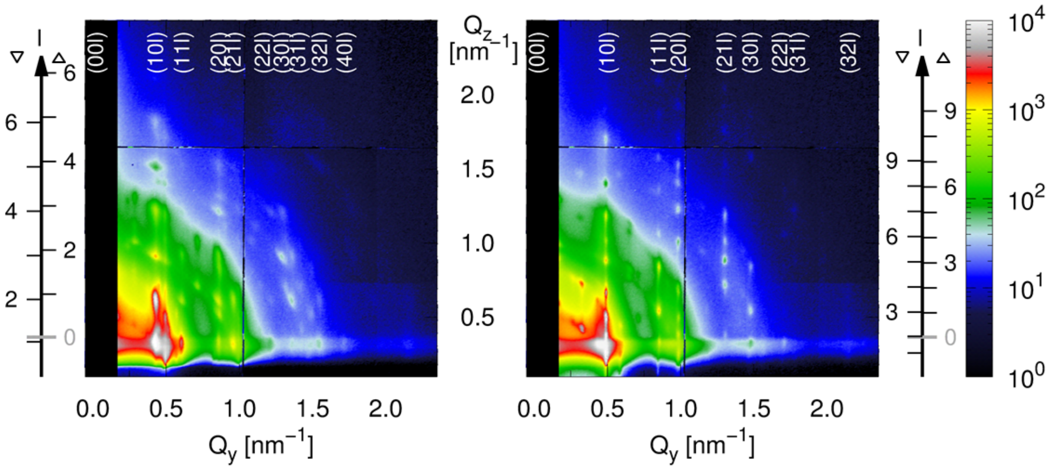

Figure S8: GISAXS by mesocrystals of highly truncated nanocubes, exhibiting preference of the tetragonal (left) and rhombohedral (right) configurations. Same data as presented in Figure 3 (main text), but without reflection markers for clarity.

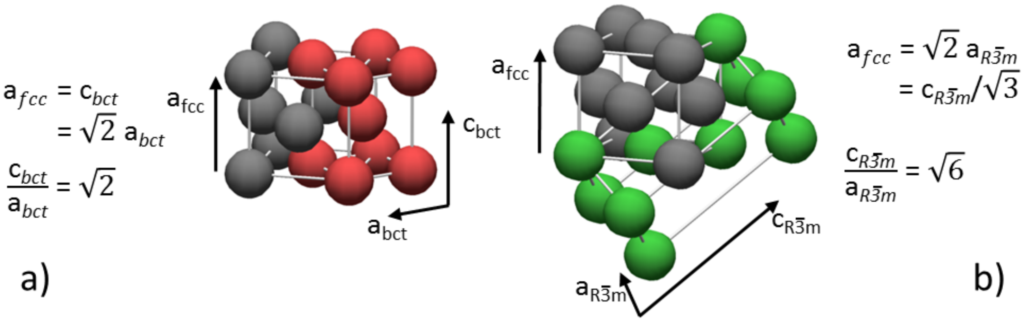

Figure S9: Geometrical relationship between an *fcc* lattice and a) *bct* (red) and b) $R\bar{3}m$ (green) lattices.

Table S3: List of GISAXS reflections positions parallel (Q_y) and perpendicular (Q_z) to the substrate as well as the lateral peak width (FWHM) for the highly truncated nanocubes mesocrystals. The pattern was measured using an incident angle of 0.3° and indexed according to $R\bar{3}m$ with a = 14.7(1) nm and c = 37.0(1) nm.

Q_y[nm^{-1}]	$Q_{y,calc}$	Q_z[nm^{-1}]	$Q_{z,calc}$	FWHM$_y$ [nm^{-1}]	*hkl* (▽)	*hkl* (△)
0.489(1)	0.492	0.262(1)	0.263	0.016(1)	(011)	
0.488(1)		0.372(1)	0.373	0.014(1)	(102)	
0.488(1)		0.502(1)	0.533	0.012(1)		(011)
0.488(1)		0.666(1)	0.700	0.011(1)		(102)
			0.702	0.011(1)	(014)	
0.487(1)		0.888(1)	0.870	0.015(1)	(105)	
0.487(1)		1.017(1)	1.037	0.017(1)		(014)
0.487(1)		1.183(1)	1.207	0.014(1)		(105)
			1.209	0.014(1)	(017)	
0.486(1)		1.406(1)	1.378	0.018(1)	(108)	
0.486(1)		1.703(1)	1.715	0.018(1)		(108)
0.323(1)	0.328	0.432(1)	0.426	0.028(2)	$(\frac{2}{3}\ 0\ \frac{7}{3})$	
0.321(1)		0.729(1)	0.756	0.031(2)		$(\frac{2}{3}\ 0\ \frac{7}{3})$
0.309(2)		1.179(1)	1.152	0.051(5)	$(\frac{2}{3}\ 0\ \frac{20}{3})$	
0.311(2)		1.473(1)	1.489	0.043(5)		$(\frac{2}{3}\ 0\ \frac{20}{3})$
0.647(2)	0.656	0.776(2)	0.758	0.04(1)	$(0\ \frac{4}{3}\ \frac{13}{3})$	
0.644(2)		0.828(2)	0.814	0.05(1)	$(\frac{4}{3}\ 0\ \frac{14}{3})$	
0.648(2)		1.08(1)	1.094	0.044(5)		$(0\ \frac{4}{3}\ \frac{13}{3})$
0.643(3)		1.14(1)	1.150	0.05(2)		$(\frac{4}{3}\ 0\ \frac{14}{3})$

Table S4: List of GISAXS reflection positions parallel (Q_y) and perpendicular (Q_z) to the substrate for the highly truncated nanocubes mesocrystals. The pattern was measured using an incident angle of 0.3° and indexed according to *I4/mmm* with a = 14.7(1) nm and c = 21.0(1) nm.

$Q_y[\mathrm{nm}^{-1}]$	$Q_{y,calc}$	$Q_z[\mathrm{nm}^{-1}]$	$Q_{z,calc}$	*hkl* (▽)	*hkl* (△)
0.4256(2)	0.4274	0.3264(5)	0.3367	(101)	
0.4263(2)		0.620(1)	0.657		(101)
0.4261(3)		0.9188(4)	0.9184	(103)	
0.4270(4)		1.218(1)	1.252		(103)
0.4254(8)		1.521(1)	1.515	(105)	
0.426(1)		1.806(3)	1.849		(105)
0.6002(5)	0.6045	0.324(1)	0.368	(110)	
			0.369		(110)
0.605(1)		0.619(1)	0.622	(112)	
0.6049(5)		0.920(1)	0.954		(112)
0.8598(5)	0.8549	0.323(1)	0.368	(200)	
			0.369		(200)
0.8550(5)		0.612(1)	0.622	(202)	
0.8547(3)		0.907(1)	0.954		(202)
0.856(1)		1.223(1)	1.216	(204)	
0.858(1)		1.526(4)	1.551		(204)
0.9564(6)	0.9558	0.3255(8)	0.3367	(211)	
0.9570(3)		0.618(1)	0.657		(211)

mined mesocrystal lattices. The particle volume of the truncated nanocubes is calculated according to

$$V_{trcube} = l_c^3 \cdot (1 - \frac{1}{6}\tau^3) \tag{S3}$$

where l_c is the cubic edge length and τ the degree of truncation. We obtain equal particle volumes for the moderately truncated nanocubes (τ_{tc} = 0.45, V_{tc} = 626(36) nm^3) and the highly truncated nanocubes (τ_{htc} = 0.88, V_{htc} = 625(51) nm^3), which justifies the proposed ageing process of dissolution and precipitation. For the nanospheres, a volume of 511(1) nm^3 is obtained using the particle radius determined by SAXS. Using the lattice parameters determined by GISAXS for the nanoparticle assemblies, we obtain packing densities of 41(2) % and 39(1) % for the *bct* packed moderately truncated nanocubes and the *fcc* packed nanospheres, respectively, as well as a much lower packing density of 28(2) % for the *fcc* packed highly truncated nanocubes.

Information on the nanocrystal orientation is not directly accessible by GISAXS, as it does not affect the structure factor but only the orientational average of the form factor of the nanocubes. Due to the arrangement of the mesocrystals in a 2D powder, this information is lost in the GISAXS pattern of the statistically averaged sample. As discussed in the main text, the low packing density of the highly truncated nanocubes justifies the assumption of at least partially aligned nanoparticles. Examples for different nanoparticle orientations are given in Figure S10. Face-to-face alignment of the highly truncated nanocubes leads to a mesocrystal structure similar to the *bct* array of the moderately truncated nanocubes as depicted in Figure S10a, with a large face-to-face separation distance of ~ 5.8 nm. Rotation of the nanocubes by 45° leads to edge-to-edge alignment of the nanocubes with an edge-to-edge separation distance of ~ 2.1 nm (Figure S10b). This separation distance is realistic and would justify the lower packing density. It is also the most simple orientation as it follows the cubic symmetry with edge-to-edge coordination in all directions, so that we chose this particle orientation for display in Figure 3 (main text). However, different particle orientations may still be feasible. The third example given in Figure S10c represents orientation of the nanoparticles with the {100} facet parallel to the [111] direction of the *fcc* mesocrystal structure, an orientation which has already been observed for larger colloids (J.-M. Meijer, Langmuir 28, 7631 (2012).). In this orientation, however, the particle separation distance are again large (≥ 5 nm), corresponding to only weak interparticle interactions.

Figure S11 shows the satellite reflections resulting from the superstructure in the [111] orientation of the *fcc* mesocrystal structure discussed in the main text (Figure 4). The additional reflections not marked in the main text result mostly from a minor contribution of the [100] orientation of the *fcc* mesocrystal structure, since in most cases both preferred orientations were present. The diffuse scattering intensity close to the (101) reflection in the Yoneda line relates to short range lateral order. This is due to a thin nanoparticle layer covering the substrate in between the mesocrystals. The nanoparticles in this thin layer are found to be partially ordered, but to a large extent disordered by SEM (not shown), resulting in a diffuse scattering contribution.

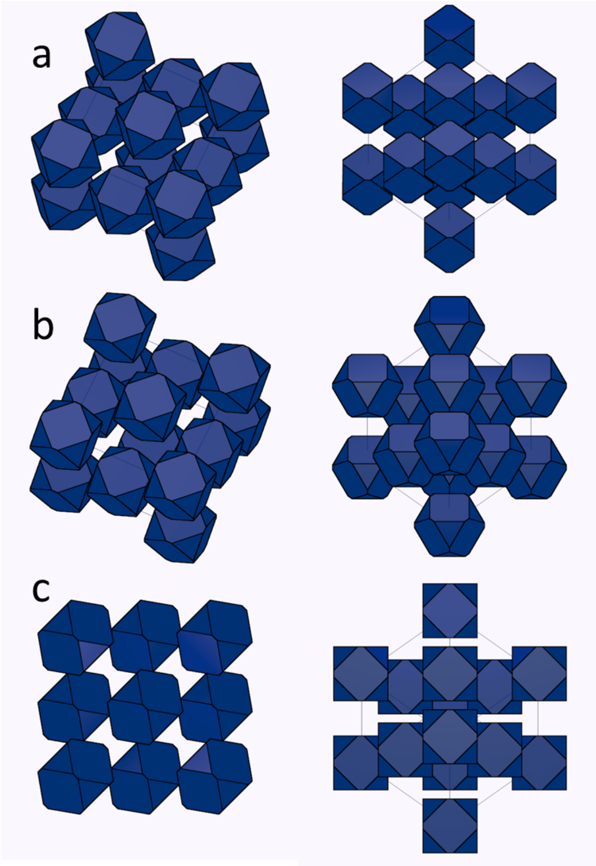

Figure S10: Examples for different nanocubes orientations in the *fcc* mesocrystal array, shown with orientation of the mesocrystal near the $[100]_{MC}$ (left) and in $[111]_{MC}$ directions (right). a) face-to-face orientation of the nanoparticles with the {100} facet parallel to the $[100]_{MC}$ direction, b) edge-to-edge orientation of the nanoparticles with the {100} facets parallel to the *fcc* unit cell edges, thus rotated in plane by 45° as compared to a), c) partial face-to-face orientation of the nanoparticles with the {100} facet parallel to one of the $[111]_{MC}$ directions.

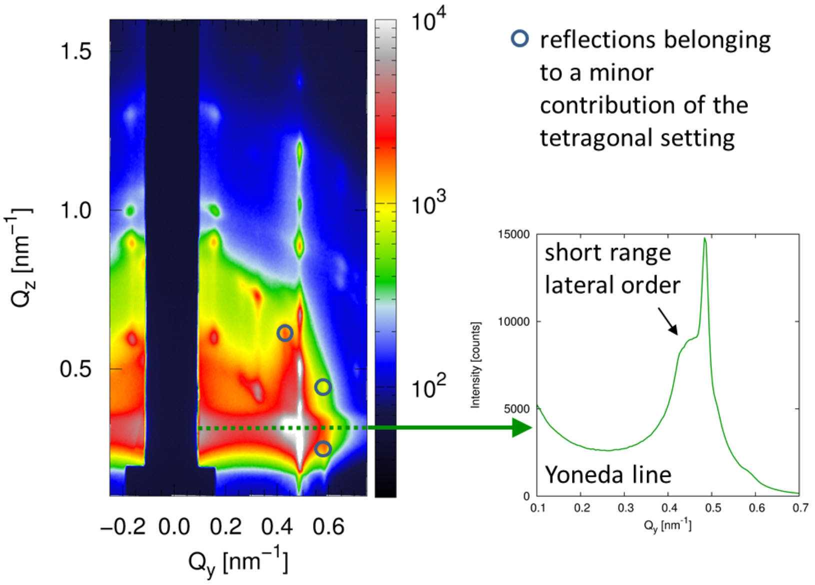

Figure S11: Detail of GISAXS data in Figure 3b (main text), indicating superstructure reflections of the (00*l*) and (10*l*) reflection series of the [111] orientation of the mesocrystals.

4.3 Superstructure reflection intensities

For quantitative evaluation of the proposed superstructure model, the structure factors of the generated reflections are calculated and compared to the relative intensities of the satellite/basic structure reflections observed using GISAXS.

The observed scattering intensity is proportional to the structure factor which is generally defined as the magnitude of the structure amplitude squared

$$I_{hkl} \sim |F_{hkl}|^2 \tag{S4}$$

with

$$F_{hkl} = \sum_j f_j \cdot e^{2\pi i (hx_j + ky_j + lz_j)} \tag{S5}$$

where f_j is the atomic form factor, h, k, l the reciprocal lattice plane indices, and x_j, y_j, z_j the positions of the atomic site j. Expansion using Euler's formula leads to

$$|F_{hkl}|^2 = \left(\sum_j f_j \cos\left(hx_j + ky_j + lz_j\right) \right)^2 + \left(\sum_j f_j \sin\left(hx_j + ky_j + lz_j\right) \right)^2 \tag{S6}$$

For determination of relative structure factors of the proposed superstructure model we calculated relative structure factors for different reciprocal lattice planes hkl and in dependence of x according to equation (S6), *i.e.* summing over all nanoparticle sites in the structure model. The atomic form factor f_j in equation (S6) was set as 1

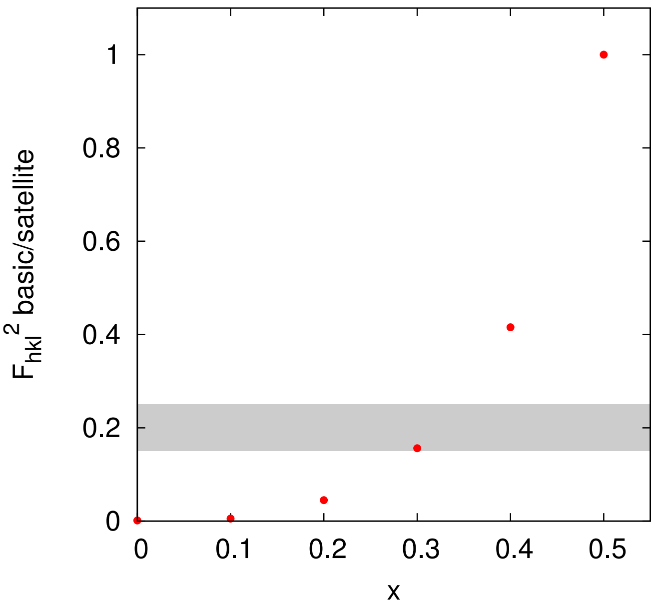

Figure S12: Satellite reflection intensities relative to the respective basis reflection depending on the relative amount of CBA stacking in the mesocrystal calculated for the proposed superstructure model. Experimentally found relative intensities are indicated as a grey shade.

(because all sites are occupied by the same nanoparticle species thus having the same scattering power), but weighted by the respective site occupancy (which depends on x for the AB and BA layers in $C\{(AB)_{1-x}(BA)_x\}C\{(AB)_{1-x}(BA)_x\}C$). We find that the structure factors of the basic reflections decrease with increasing x, whereas the structure factors of the superstructure reflections increase simultaneously. The ratio of the satellite/basic reflection structure factors is presented in Figure S12.

Due to reflection overlap in the GISAXS pattern, only a few pairs of basic reflection and superstructure satellite are accessible experimentally for intensity determination. Furthermore, a direct comparison of the observed reflection intensities is likely affected by additional uncertainty resulting from a different reflectivity at different Q_z as well as an unknown distribution of populations of the different monoclinic domains in the entire mesocrystals. However, for the pairs of (4/3 0 14/3)/(1 0 5), without reflection at the substrate, (0 4/3 13/3)/(0 1 4), and (4/3 0 14/3)/(1 0 5), both with reflection at the substrate, individual intensities were accessible. We find relative satellite intensities of 0.24(2), 0.25(2), and 0.14(3), respectively, which are in the correct order of magnitude to correspond to the proposed superstructure model (see grey shade in Figure S12). Comparison of the calculated and observed relative intensities suggests a relative amount of the superstructure of $0.3 < x < 0.35$ in the studied mesocrystal sample. In this model, x does not indicate the amount of stacking faults, but the relative amount of CBACBA stacking in the mesocrystal sample, here 30 - 35%. Thus, it is not to be taken as an indication whether there are large ($x = 0$) and ($x = 1$) domains or a random order of CABC and CBAC units in the mesocrystal.

A comparison of the lateral width of the reflections (see Table S3) implies that the correlation length of the superstructure is 2-3 times shorter than that of the parent structure. This is in agreement with observations in SEM images of smaller domains with linear defects embedded into the larger mesocrystals with parent structure. The still large correlation length indicates the presence of large domains in the mesocrystals as induced by only few stacking faults.